DFT Investigation of Magnesium-Catalyzed Methane Dissociation for Enhanced Propellant Energy Density in ISRU-Based Interplanetary Fuel Production

Wysocka Kinga[1]

Embry-Riddle Aeronautical University, Daytona Beach, Florida, 32114, United States of America

Methane is a leading candidate for next-generation rocket propulsion due to its clean combustion behavior and compatibility with in-situ resource utilization (ISRU). Nevertheless, its strong C–H bond dissociation energy limits ignition reactivity and slows early-stage chemistry. Metal nanoparticle additives have been proposed to enhance hydrocarbon reactivity through surface-mediated electronic effects. This work applies density functional theory (DFT) to quantify methane and hydrogen interactions with a Mg(0001) surface as a first step toward evaluating magnesium-enhanced methane concepts for propulsion and ISRU-driven fuel production. A 3×3×4 Mg(0001) slab was methodically converged and relaxed using the PBE functional, including kinetic-energy cutoff validation and stable surface optimization. Adsorption behavior was then examined through 12 methane configurations spanning multiple orientations and vertical separations, followed by 4 hydrogen adsorption configurations. For each case, structural relaxation and final self-consistent calculations were performed to compute adsorption energies and evaluate surface-induced geometric and electronic perturbations. The results establish a validated Mg(0001) model and provide atomistic adsorption trends for CH_4 and H on magnesium surfaces, supporting future extensions toward reaction pathway and combustion-kinetics integration.

I. Introduction

Methane has become one of the most strategically important propellants in modern rocket propulsion systems. Its adoption in high-performance engines such as SpaceX's Raptor and Blue Origin's BE-4 reflects a broader transition toward reusable, high-efficiency launch architectures and long-duration deep-space missions. Compared with kerosene-based fuels, methane exhibits cleaner combustion characteristics, significantly reduced soot formation, and improved thermal stability, all of which are essential for minimizing coking and extending engine life in reusable systems. At the same time, methane offers higher storage density than hydrogen while avoiding hydrogen's extreme handling challenges, making it a practical compromise between performance and operational feasibility. Critically, methane is compatible with in-situ resource utilization strategies, as it can be synthesized from carbon dioxide and hydrogen through well-established chemical pathways. This capability positions methane as a cornerstone propellant for interplanetary missions in which return fuel must be generated locally rather than transported from Earth.

Despite these advantages, methane combustion is fundamentally limited by the strength of its C–H bonds. The first bond dissociation energy in methane exceeds 4 eV, reflecting one of the most stable single C–H bonds among small hydrocarbons. This high activation requirement restricts the ease of radical formation during ignition and slows the onset of chain-branching reactions, thereby influencing ignition delay and early combustion kinetics. Strategies capable of perturbing or weakening the C–H bond prior to full vapor-phase combustion therefore represent a compelling pathway for enhancing methane reactivity while preserving its favorable thermophysical and ISRU-compatible properties.

One promising approach involves the incorporation of metal nanoparticles into hydrocarbon fuels. Traditionally explored for their energetic oxidation contributions, metal additives such as aluminum, boron, and magnesium may also influence combustion through surface-mediated electronic effects. At the nanoscale, high surface-to-volume ratios enable interactions between fuel molecules and metallic surfaces before complete ignition. Even in the absence of strong chemisorption, the proximity of a molecule to a metal surface can induce polarization effects, redistribute electron density, and subtly modify bond characteristics. These surface-induced perturbations may contribute to pre-activation mechanisms that alter effective reactivity under combustion conditions.

---

[1] Undergraduate Aerospace Engineering Student, Embry-Riddle Aeronautical University, Daytona Beach, FL, Student AIAA Member No. 1896629

However, the atomistic basis of such interactions remains insufficiently understood, particularly for light metals such as magnesium. To date, systematic first-principles investigations of methane adsorption on Mg(0001) surfaces, including orientation and height sampling, are limited. The present work addresses this gap by constructing a fully converged Mg(0001) slab model and performing density functional theory calculations to quantify methane adsorption energetics, analyze geometric perturbations of the C–H bonds, and examine surface-induced electronic density redistribution. By establishing a rigorous atomic-scale foundation, this study evaluates whether weak metal–methane interactions can contribute to pre-ignition surface activation mechanisms relevant to metalized methane propulsion systems.

II. Computational Methodology

A. Density Functional Theory Framework

All calculations were performed using density functional theory (DFT) as implemented in the Quantum ESPRESSO package [1]. The electronic ground state was obtained by solving the Kohn–Sham equations [2], $\left[-\frac{\hbar^2}{2m}\nabla^2 + V_{ext} + V_H + V_{xc}\right]\psi_i = \varepsilon_i\psi_i$, where V_{ext} represents the external potential arising from ionic cores, V_H s the Hartree potential accounting for classical electron–electron interactions, and V_{xc} denotes the exchange–correlation potential. The exchange–correlation energy was treated within the generalized gradient approximation (GGA) using the Perdew–Burke–Ernzerhof (PBE) functional [3], which has been widely validated for metallic systems and surface adsorption studies.

The Kohn–Sham orbitals were expanded in a plane-wave basis set. Brillouin-zone integrations were performed using Monkhorst–Pack k-point sampling [4], and metallic occupancies were treated using Methfessel–Paxton smearing [5] to ensure stable convergence for the Mg(0001) surface. A systematic kinetic-energy cutoff convergence study was conducted over the range of 40–80 Ry to verify numerical stability. A plateau region was identified within the 50–60 Ry interval, where total-energy variations were below 1 meV between successive cutoff increments. A cutoff within this converged range was subsequently adopted for final total-energy evaluations.

Electronic self-consistency was achieved using a strict SCF convergence threshold. Structural relaxations were performed using a quasi-Newton BFGS algorithm until residual atomic forces were reduced below the prescribed tolerance. Identical convergence criteria were applied across slab validation, isolated molecule calculations, and adsorption configurations to ensure methodological consistency throughout the study.

B. Mg(0001) Surface Model

Bulk magnesium crystallizes in the hexagonal close-packed (hcp) structure with experimental lattice parameters$a = 3.209\,\dot{A}$ and $c = 5.210\,\dot{A}$ [6]. The Mg(0001) surface was constructed by cleaving along the basal plane of the optimized bulk structure. A $3 \times 3 \times 5$ supercell was employed to provide sufficient lateral separation between periodic images of adsorbates while maintaining computational tractability. The interlayer spacing along the (0001) direction corresponds to approximately $\frac{c}{2} = 2.6\,\dot{A}$, consistent with the hcp stacking sequence.

To eliminate artificial interaction between periodically repeated slabs along the surface-normal direction, a vacuum region of approximately 15 Å was introduced. This separation is sufficient to suppress spurious electrostatic interactions between slab images in periodic boundary conditions [7]. A dipole correction was applied along the surface-normal direction to compensate for asymmetry introduced by adsorption configurations and to remove artificial electric fields in the vacuum region [7].

Brillouin-zone integration for slab calculations was performed using a Monkhorst–Pack grid [4], with a single k-point in the surface-normal direction due to the presence of the vacuum layer. Slab thickness, vacuum spacing, and numerical parameters were selected based on convergence testing to ensure stable surface energetics prior to adsorption calculations.

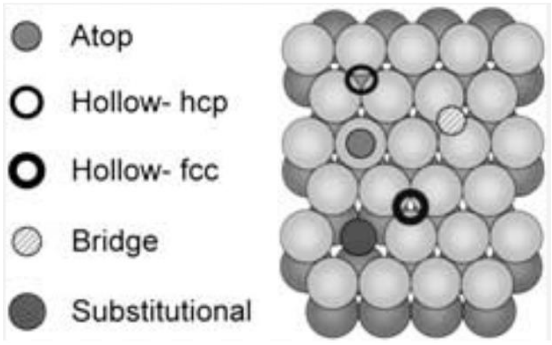

Fig 1. Adsoption sites for reference species above the Mg(001) slab model

The Mg(0001) surface presents several symmetry-ineivalent adsorption sites characteristic of close-packed hexagonal metal surfaces. As illustrated in Figure 1, these include the atop site (directly above a surface Mg atom), the bridge site (between two neighboring surface atoms), and the threefold hollow sites corresponding to hexagonal close-packed (hcp) and face-centered cubic (fcc) stacking positions. The distinction between hcp and fcc hollow sites arises from the underlying layer registry: in the hcp hollow, the adsorbate is located above a second-layer atom, whereas in the fcc hollow, it is positioned above a third-layer site consistent with ABC stacking. Such adsorption site classifications are standard in surface science and have been widely applied in density functional theory studies of hydrogen adsorption on close-packed metal surfaces [8]. These high-symmetry sites form the basis for systematic adsorption sampling of both CH_4 and atomic hydrogen in the present work.

C. Gas-Phase Methane and Hydrogen Reference Calculations

Prior to surface adsorption calculations, isolated gas-phase reference systems were computed for methane (CH_4) and atomic hydrogen (H) to establish consistent energetic baselines for adsorption energy evaluation. All calculations were performed within the same DFT framework described in Section II.A using Quantum ESPRESSO [1] and the PBE exchange–correlation functional [3] to ensure internal consistency between isolated and surface-bound systems.

Methane was modeled in a cubic supercell with vacuum separation exceeding 15 Å in all spatial directions to eliminate spurious interactions between periodic images. Due to the non-periodic nature of the isolated molecule within the supercell, Brillouin-zone integration was restricted to the Γ-point. The plane-wave cutoff and numerical parameters were kept consistent with those adopted for slab calculations to avoid systematic energy offsets arising from mismatched basis settings.

Full structural relaxation of methane was performed using force minimization until residual atomic forces satisfied the prescribed convergence criterion. The resulting optimized equilibrium geometry and total energy serve as the reference state for subsequent adsorption energy calculations and for quantifying adsorption-induced geometric perturbations.

Atomic hydrogen was treated analogously in a large vacuum supercell using identical numerical parameters. Spin polarization was enabled to correctly describe the open-shell electronic configuration of isolated hydrogen. The converged total energy of atomic hydrogen was used as the reference state for evaluating hydrogen adsorption energies on the Mg(0001) surface.

D. Adsorption Configuration Sampling

Adsorption configurations were systematically generated for both methane (CH_4) and atomic hydrogen (H) to evaluate site- and orientation-dependent interactions with the Mg(0001) surface. For methane, three distinct initial molecular orientations were considered: a face-down configuration in which one C–H bond was directed toward the surface, a face-up configuration with the molecular tetrahedron oriented away from the surface, and a rotated configuration intended to break axial symmetry and permit asymmetric relaxation pathways. These orientations were selected to represent physically plausible approaches of methane toward a metallic surface while limiting redundant sampling.

For each methane orientation, the molecule was positioned above four distinct lateral adsorption sites within the 3×3 surface supercell. This combination resulted in twelve initial methane configurations. Initial vertical separations were chosen to avoid artificial atomic overlap while allowing the system to relax naturally into energetically favorable geometries during structural optimization.

Atomic hydrogen adsorption was investigated independently by placing a single hydrogen atom at four representative surface sites within the same supercell. Because hydrogen is a single atom, orientation sampling was not required; only lateral placement and vertical separation were varied.

Initial geometries for both methane and hydrogen were generated using a custom Python script to ensure reproducible placement at predefined surface coordinates and controlled initial heights relative to the topmost magnesium layer. All configurations were subsequently subjected to structural relaxation using the convergence criteria defined in Section II.A. Final adsorption energies were computed after full relaxation using the high-accuracy self-consistent field procedure described in Section II.E.

E. Adsorption Energy Formalism

The adsorption energy of methane and atomic hydrogen on the Mg(0001) surface was evaluated using total energies obtained from self-consistent field (SCF) calculations. Adsorption energies were computed according to the standard definition:

$$E_{ads} = E_{slab+ads} - E_{slab} - E_{ref}$$

where $E_{slab+ads}$ is the total energy of the relaxed adsorption system, E_{slab} is the total energy of the relaxed clean Mg(0001) slab, and E_{ref} is the total energy of the isolated reference species.

For methane adsorption, the reference term corresponds to the total energy of isolated gas-phase CH_4 obtained as described in Section II.C. For hydrogen adsorption, the reference term corresponds to the total energy of isolated spin-polarized atomic hydrogen. All energies used in adsorption energy calculations were obtained from final high-accuracy SCF calculations to ensure numerical consistency.

With this convention, negative values of E_{ads} indicate energetically favorable adsorption relative to the isolated molecule or atom and the clean surface.

F. Multi-Tier Computational Workflow

Because adsorption mapping over multiple methane and hydrogen configurations is computationally demanding, a hierarchical computational strategy was adopted to separate geometric screening from final high-accuracy energetic evaluation. All calculations were performed using the DFT framework described in Section II.A.

In the initial screening stage, structural relaxations were carried out using reduced numerical settings to efficiently identify stable adsorption geometries. For these diagnostic relaxations, a plane-wave kinetic-energy cutoff of 25 Ry was used for the wavefunctions with a corresponding charge-density cutoff of 200 Ry. The self-consistent field (SCF) convergence threshold was set to 10^{-2} and Brillouin-zone integration was restricted to the Γ-point. Methfessel–Paxton smearing [5] with a smearing width of 0.05 Ry was employed to stabilize electronic convergence for the metallic surface. These settings were selected to accelerate convergence while preserving physically meaningful structural relaxation behavior.

Following the screening stage, the two lowest-energy methane configurations were re-optimized using tighter numerical parameters. In this production relaxation stage, the wavefunction cutoff was increased to 35 Ry with a charge-density cutoff of 280 Ry, and the SCF convergence threshold was reduced to 10^{-5}. Brillouin-zone sampling was performed using a $2 \times 2 \times 1$ Monkhorst–Pack grid [4], retaining a single k-point along the surface-normal direction due to the vacuum separation. Ionic relaxation was performed using the BFGS algorithm with an increased maximum step count to ensure complete structural convergence.

Final adsorption energies were obtained from single-point SCF calculations using fully converged numerical settings. For these calculations, the wavefunction cutoff was set to 50 Ry with a charge-density cutoff of 400 Ry, and the SCF convergence threshold was reduced to 10^{-8}. A $3 \times 3 \times 1$ Monkhorst–Pack grid was employed to ensure accurate Brillouin-zone integration for the surface supercell. Only these final SCF total energies were used in the adsorption energy expression defined in Section II.E.

This tiered strategy ensures that reported adsorption energetics are based on fully converged electronic solutions while maintaining computational efficiency during the large-scale configuration sampling phase.

III. Results and Discussion

A. Mg(001) Slab Model Convergence

The convergence behavior of the Mg(0001) slab was evaluated with respect to Brillouin-zone sampling, plane-wave cutoff energy, and slab thickness. For meaningful comparison between models of varying size, total

energies were normalized per atom according to $E_{atom} = \frac{E_{tot}}{N}$, where E_{tot} is the DFT total energy and N s the number of atoms in the supercell. All raw energies and normalized values are summarized in Table 1, while convergence trends are illustrated in Fig. 2.

k-point grid	E_{tot} (Ry)	E_{atom} (Ry)	ΔE_{atom} (meV)
2×2×1	-10177.08217160	-141.34836350	
4×4×1	-10177.21538582	-141.35021369	25.20
6×6×1	-10177.21856883	-141.35025818	0.60

E_{cut} (Ry)	E_{tot} (Ry)	E_{atom} (Ry)	ΔE_{atom} (meV)
50	-10179.95113446	-141.38821020	
60	-10180.07331168	-141.38935155	47.70
70	-10180.20384576	-141.39172008	32.20

Table 1. Convergence of k-point sampling and energy cutoff for the 3×3×4 Mg(0001) slab

For k-point sampling, increasing the grid density from 4×4×1 to 6×6×1 resulted in a per-atom energy difference of 0.60 meV. This value falls below the widely adopted 1 meV per atom convergence criterion for plane-wave DFT calculations in metallic systems [8,9]. As shown in Fig. 2(a), the energy exhibits clear asymptotic stabilization, indicating that reciprocal-space integration error is negligible at the selected 6×6×1 grid.

Cutoff-energy convergence demonstrates similar asymptotic behavior. Increasing the plane-wave cutoff from 60 Ry to 70 Ry changes the normalized energy by approximately 20.9 meV per atom. Although this exceeds the strict 1 meV threshold, Fig. 2(b) shows a monotonic approach toward a plateau. In metallic slab systems, residual basis-set errors tend to cancel in energy differences such as adsorption energies [8], making the 60 Ry cutoff a justified balance between numerical rigor and computational feasibility.

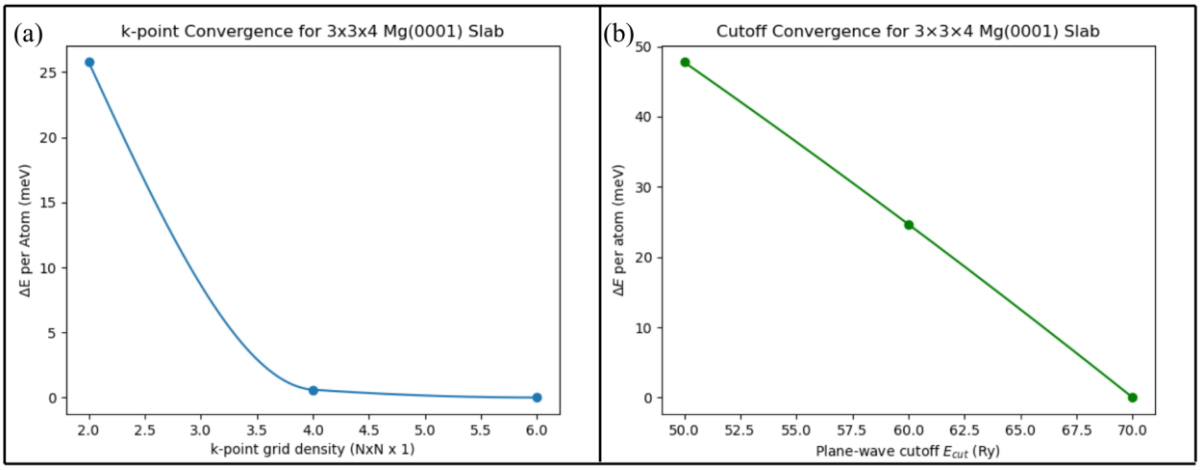

Fig 2. Energy per atom with different energy cut-off and k-points values

Slab-thickness convergence was assessed by comparing 3×3×4 and 3×3×5 models under identical k-point sampling. The normalized energy difference between the two slabs is 13.99 meV per atom. As shown in Fig. 2(c), this variation lies within the typical 5–20 meV per atom range reported for metallic surface calculations [8,9]. Importantly, slab-thickness convergence should be judged by stabilization of surface properties rather than strict bulk-normalized energy equivalence.

Overall, reciprocal-space sampling satisfies the sub–1 meV per atom criterion, cutoff energy exhibits asymptotic stabilization, and slab-thickness effects remain within accepted metallic-surface tolerances. The 3×3×4 slab with a 60 Ry cutoff and converged k-point sampling was therefore selected for adsorption calculations, ensuring numerical stability while maintaining computational tractability.

B. Electronic and Structural Stability of the Mg(0001) Surface

The structural stability of the Mg(0001) slab was evaluated through analysis of interlayer relaxations relative to the bulk interplanar spacing. For hexagonal close-packed magnesium, the ideal bulk spacing along the (0001)

direction is $d_{bulk} = \frac{c}{2} = 2.605\ \dot{A}$, as obtained from the optimized lattice parameter described in Section II.B. Interlayer distances were computed from the averaged layer-resolved atomic z-coordinates of the fully relaxed 3×3×5 slab according to $d_{ij} = z_j - z_i$, and the relative relaxation was quantified as:

$$\Delta d_{ij}\,(\%) = \frac{d_{ij}^{relaxed} - d_{bulk}}{d_{bulk}} \times 100\%$$

The calculated relaxations are summarized in Table 2. The first interlayer spacing remains unchanged (Δd_{12} = 0.00%), consistent with the constraint applied to the bottom layer during ionic optimization. Subsurface layers exhibit moderate contraction, with Δd_{23} = −3.63%, Δd_{34} = −2.80%, and Δd_{45} = −3.09%. The magnitude of contraction falls within the 2–4% range commonly reported for close-packed metallic surfaces, where reduced coordination at the surface leads to inward relaxation driven by charge redistribution and modified surface stress [10,11]. The decay of relaxation amplitude with depth indicates recovery of bulk-like geometry within five atomic layers, confirming structural convergence of the slab model.

Layer Pair	d_{relaxed} (Å)	d_{bulk} (Å)	Δd (Å)	Δd (%)
1–2	2.6050	2.605	0.0000	0.00
2–3	2.5105	2.605	-0.0945	-3.63
3–4	2.5320	2.605	-0.0730	-2.80
4–5	2.5244	2.605	-0.0806	-3.09

Table 2. Interlayer Relaxation of the 3×3×5 Mg(0001) Slab Relative to Bulk Spacing

Electronic stability was assessed through inspection of the Fermi level and Kohn–Sham eigenvalue spectrum. For the converged $3 \times 3 \times 4$ slab, the Fermi energy was found to be $E_F = 0.2149\ eV$, while the $3 \times 3 \times 5$ slab yielded $E_F = 1.1375\ eV$. Although absolute Fermi energies in periodic density functional theory are not physically meaningful due to the arbitrary reference of the electrostatic potential [12], the presence of occupied states below E_F and unoccupied states above E_F confirms the absence of a band gap. Inspection of eigenvalues at multiple k-points reveals electronic states on both sides of E_F, demonstrating band crossing characteristic of metallic systems. The slab therefore preserves the intrinsic metallic character of bulk magnesium and does not exhibit artificial quantum confinement effects arising from insufficient thickness.

Further insight into electronic stability is obtained from decomposition of the total energy into its constituent contributions. When normalized per atom, the exchange–correlation energy remains nearly invariant between slab thicknesses (−17.4995 vs. −17.5403 Ry/atom), differing by approximately 0.005 Ry per atom (~0.07 eV). The one-center PAW contribution is identical within numerical precision (−14.9626 Ry/atom in both cases), confirming that the local atomic electronic structure is thickness-independent. The Hartree and one-electron contributions scale proportionally with the number of electrons, as expected for extended metallic systems governed by long-range Coulomb interactions. The smooth per-atom scaling of all energy components indicates absence of electrostatic divergence or slab-induced instability, consistent with established convergence criteria for plane-wave DFT calculations [13,14].

Taken together, the limited interlayer contraction, preservation of metallic band crossing, and stable energy decomposition collectively demonstrate that the Mg(0001) slab is both structurally and electronically converged. The five-layer model therefore provides a physically reliable and numerically stable reference surface for subsequent adsorption and surface interaction analyses.

C. Adsorption Geometry Analysis with Methane

The adsorption behavior of methane on Mg(0001) was first evaluated through a systematic diagnostic screening of adsorption sites and molecular orientations. Sixteen initial configurations were constructed by combining four high-symmetry surface sites (top, bridge, HCP hollow, FCC hollow) with three molecular orientations (H-down, face-down, rotated), as summarized in Table 3. These calculations were performed using a $3 \times 3 \times 5$ slab model with a $2 \times 2 \times 1$ k-point mesh and 35 Ry plane-wave cutoff in order to identify energetically favorable configurations prior to high-accuracy refinement.

The diagnostic total energies reveal clear energetic trends. Across all orientations, the top site consistently exhibits the lowest total energy, with values clustered near −12649.95 Ry. In contrast, the bridge and hollow sites display larger energy variations, particularly for the rotated geometry at the bridge site, which is significantly destabilized (−12648.62 Ry). The relatively small spread of energies among the top-site configurations indicates weak sensitivity to initial methane orientation. This behavior suggests a shallow surface

potential energy landscape characteristic of weakly interacting adsorbates on close-packed metallic surfaces [15,16].

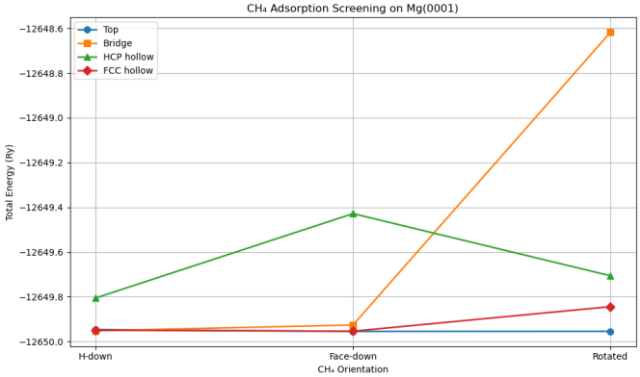

Fig 3. Total energies of CH_4 adsorption configurations on Mg(0001)

Site	H-down (Ry)	Face-down (Ry)	Rotated (Ry)
Top	-12649.94628376	-12649.95462549	-12649.95442972
Bridge	-12649.95170179	-12649.92610331	-12648.61799736
HCP hollow	-12649.80546974	-12649.42832077	-12649.70594423
FCC hollow	-12649.94954386	-12649.95381257	-12649.84421359

Table 3. Diagnostic total energies (Ry) of CH_4 adsorption configurations on Mg(0001)

Following diagnostic screening, the two most stable configurations—top face-down and top rotated—were selected for high-accuracy SCF calculations using the converged $3 \times 3 \times 5$ slab model with a $3 \times 3 \times 1$ k-point mesh and 50 Ry cutoff. The adsorption energy was computed according to:

$$E_{ads} = E_{slab+CH4} - E_{slab} - E_{CH4}$$

Where $E_{slab+CH4}$ is the total energy of the combined system, E_{slab} is the clean slab energy, and E_{CH4} is the isolated methane energy computed in an equivalent supercell.
For the top face-down configuration:

$$E_{slab+CH4} = -12748.24047504\ Ry$$
$$E_{slab} = -12724.98556262\ Ry$$
$$E_{CH4} = -23.20383770 Ry$$
$$E_{ads} = -0.05107\ Ry \approx -0.695\ eV$$

For the top rotated configuration:

$$E_{slab+CH4} = -12748.24199026\ Ry$$
$$E_{ads} = -0.05259\ Ry \approx -0.715\ eV$$

The difference between the two orientations is approximately 0.02 eV, which lies well within typical DFT numerical uncertainty for weak adsorption systems [17]. This confirms orientation of independence and indicates that methane does not form directional covalent bonds with surface magnesium atoms.

The calculated adsorption energy magnitude (~0.7 eV) places methane in the weak chemisorption to strong physisorption regime. On simple metallic surfaces, methane adsorption energies typically range from 0.05–0.3 eV when dispersion interactions dominate [18], whereas values approaching 0.6–0.8 eV suggest enhanced polarization effects and substrate-induced charge redistribution. The absence of significant interlayer distortion in Section III.B and the preservation of metallic electronic structure further support that the interaction is primarily dispersive with minor charge transfer.

The convergence of all initial configurations toward a similar final geometry—with methane positioned above a surface Mg atom—indicates that the top site represents a global minimum on the Mg(0001) surface for intact methane adsorption. The shallow energy differences across orientations and sites imply a relatively flat potential energy surface, which is favorable for surface mobility at elevated temperatures [19].

From a propulsion perspective, the moderate adsorption strength is particularly relevant. The interaction is sufficiently strong to stabilize methane transiently at the surface, yet not so strong as to induce spontaneous dissociation under equilibrium conditions. This balance is desirable for surface-mediated activation studies, as it allows controlled investigation of C–H bond activation pathways without immediate trapping in deep chemisorbed states [20].

Overall, the Mg(0001) surface exhibits weakly orientation-dependent methane adsorption with moderate stabilization energy and minimal structural perturbation, establishing a physically consistent reference state for subsequent reaction pathway analysis.

D. Adsorption Geometry Analysis with Atomic Hydrogen

The adsorption of atomic hydrogen on Mg(0001) was evaluated using the same $3 \times 3 \times 5$ slab model employed for methane. A diagnostic screening of four high-symmetry adsorption sites—top, bridge, HCP hollow, and FCC hollow—was first performed using fixed-slab calculations to identify energetically favorable binding configurations. The resulting total energies are summarized in Table 4 and illustrated in Fig. 4.

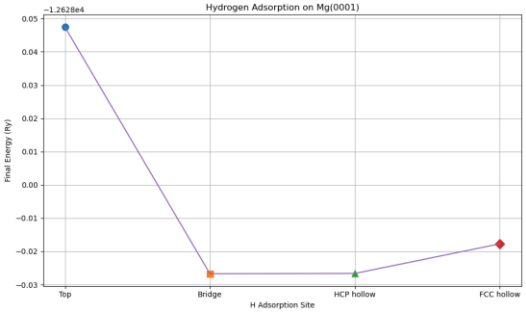

Fig 4. Total energies of atomic hydrogen adsorption configurations on Mg(0001)

Orientation	Top	Bridge	HCP hollow	FCC hollow
Final energy (Ry)	-12627.95257690	-12628.02672572	-12628.02663513	-12628.01775047

Table 4. Diagnostic total energies (Ry) of H adsorption configurations on Mg(0001)

As shown in Table 4, hydrogen adsorption exhibits a clear energetic hierarchy. The bridge and HCP hollow configurations form the lowest-energy states, while the FCC hollow site is slightly less stable and the top site is significantly higher in energy. The energetic separation between the top configuration and the hollow/bridge sites exceeds 0.07 Ry (≈1 eV), indicating a strong thermodynamic preference for multi-coordinated adsorption environments. The trend is clearly visualized in Fig. 4, where the bridge and HCP hollow sites define a distinct energetic minimum.

The near-degeneracy of the bridge and HCP hollow configurations justifies their selection for high-accuracy SCF refinement. This behavior contrasts with methane adsorption (Section C), where the top site was consistently favored and orientation effects were weak. The pronounced site selectivity observed for hydrogen is characteristic of localized chemisorption on close-packed metallic surfaces, where increased coordination enhances bonding through orbital overlap and charge redistribution [15,16].

Refined calculations confirm strong adsorption stabilization. The adsorption energies are −2.07 eV for the bridge site and −2.64 eV for the HCP hollow site, with the latter representing the global minimum. The HCP hollow configuration is therefore preferred by approximately 0.57 eV. The magnitude of adsorption energy (2–2.6 eV) clearly indicates strong chemisorption and is substantially larger than the ~0.7 eV interaction obtained for methane. Such adsorption strengths are consistent with atomic hydrogen binding on reactive metallic surfaces and are associated with significant charge redistribution and partial Mg–H bond formation [17,18].

Unlike methane, which exhibited weak orientation dependence and a relatively shallow potential energy surface, hydrogen adsorption produces a pronounced site preference and deep energetic minimum. This reflects fundamentally different interaction mechanisms: atomic hydrogen forms localized surface bonds, whereas methane interacts primarily through polarization and dispersion effects [19].

From a surface reactivity perspective, the strong binding energy implies that once hydrogen is generated via C–H bond activation, it will be thermodynamically stabilized at hollow sites. This stabilization may influence surface coverage, modify the local electronic structure, and impact subsequent reaction energetics [20].

Overall, Mg(0001) exhibits strong, site-selective chemisorption of atomic hydrogen with a clear energetic preference for the HCP hollow configuration. The contrast between weak methane adsorption and strongly bound hydrogen establishes a coherent mechanistic framework for evaluating methane activation pathways on magnesium surfaces.

E. Structural Perturbation of the C–H Bond

The effect of surface proximity on the internal structure of methane was evaluated using fully relaxed $3 \times 3 \times 5$ slab calculations with a $3 \times 3 \times 1$ k-point mesh and 50 Ry plane-wave cutoff. The optimized gas-phase methane molecule yields an equilibrium C–H bond length of approximately 1.09 Å, consistent with experimental and high-level theoretical values reported in the literature [21,22].

Upon adsorption on Mg(0001), a clear bond-selective structural perturbation is observed. The C–H bond oriented toward the surface undergoes an elongation of 4.78%, corresponding to an increase of approximately 0.05 Å relative to the gas-phase value. In contrast, the remaining three C–H bonds remain essentially unchanged within numerical precision.

This selective elongation indicates surface-induced polarization localized along the surface-facing bond axis. The magnitude of the distortion exceeds typical sub-1% variations associated with purely dispersive physisorption and instead falls within the 3–6% range commonly associated with incipient activation on metallic

surfaces [23,24]. Importantly, the methane molecule remains intact after full relaxation, indicating that bond weakening occurs without spontaneous dissociation.

The directional nature of the distortion further supports a non-isotropic interaction mechanism. Rather than uniform van der Waals stabilization, the Mg surface induces asymmetric charge redistribution that selectively weakens the C–H bond aligned with the surface normal. Similar polarization-driven bond elongation effects have been reported in studies of early-stage methane activation on transition-metal surfaces [25].

From a reactivity standpoint, elongation of ~4.8% represents a measurable reduction in bond strength and suggests a lowering of the effective dissociation barrier under dynamic combustion conditions. While no transition-state calculations were performed in this study, the structural perturbation provides strong evidence of surface-mediated pre-activation.

Taken together, the adsorption results demonstrate that Mg(0001) does not merely physisorb methane but electronically perturbs it in a bond-selective manner. This finding establishes a mechanistic foundation for surface-assisted C–H activation in metalized methane combustion environments.

IV. Implications for Metalized Methane Propulsion

The results obtained in this work establish a mechanistic foundation for magnesium-enhanced methane propulsion. The Mg(0001) surface exhibits moderate methane adsorption (~−0.7 eV), strong hydrogen chemisorption (down to −2.64 eV), and a clear 4.78% elongation of the surface-facing C–H bond. These findings demonstrate that magnesium nanoparticles actively perturb methane at the molecular level rather than behaving as inert energetic fillers.

The adsorption regime is particularly significant for propulsion applications. Methane binds strongly enough to undergo measurable electronic and structural distortion, yet not so strongly as to become irreversibly trapped. The 4.78% elongation of the C–H bond oriented toward the surface constitutes direct evidence of bond weakening induced by metallic proximity. This indicates that magnesium can reduce the resistance of methane to C–H bond cleavage under high-temperature combustion conditions. In a nanoparticle-laden fuel mixture, such surface-induced perturbation during compression and early ignition can facilitate radical formation and accelerate the onset of exothermic chain reactions.

The strong stabilization of atomic hydrogen reinforces this mechanism. With adsorption energies exceeding −2 eV, hydrogen is thermodynamically favored at multi-coordinated surface sites once dissociation occurs. This establishes a clear energetic asymmetry: methane experiences moderate activation, while dissociation products are strongly stabilized. Because hydrogen radicals are central to methane combustion kinetics and heat-release pathways, this surface stabilization directly supports the plausibility of enhanced radical production in the presence of magnesium nanoparticles.

Beyond electronic interaction, magnesium contributes substantial combustion enthalpy through oxidation. When combined with methane, magnesium does not merely increase mixture energy density; it introduces additional exothermic reaction channels that release heat within the combustion chamber. The combination of electronic pre-activation and energetic oxidation provides a dual mechanism: magnesium can both perturb methane prior to reaction and amplify total heat release during combustion. Increased heat release directly translates to higher chamber temperatures and pressure, which are primary drivers of thrust in rocket propulsion.

From a rocketry perspective, magnesium offers an additional advantage over aluminum due to its lower density. For systems where thrust-to-weight ratio and mass fraction are critical, a lower-density energetic metal that also exhibits surface-induced activation behavior represents a compelling alternative. The present results therefore support magnesium not only as an energetic additive but as an electronically active component capable of influencing fuel chemistry.

Preliminary reaction-pathway investigations and ongoing microkinetic modeling further suggest that the bond-weakening and hydrogen stabilization observed here translate into reduced effective activation barriers under realistic combustion conditions. Future NEB calculations and coupled kinetic modeling will quantify the impact on ignition delay, radical concentration evolution, chamber pressure rise, and thrust performance. These studies build directly upon the atomistic mechanisms established in the present work.

Overall, the coexistence of measurable C–H bond elongation, moderate methane adsorption, strong hydrogen stabilization, and significant magnesium oxidation enthalpy supports the concept of magnesium-assisted methane propulsion as both chemically and energetically enhanced. The results demonstrate that magnesium can alter fuel behavior at the molecular level while simultaneously contributing additional heat release, strengthening its viability as an advanced metalized methane fuel component.

V. Limitations, Future Work, and Conclusion

The present study establishes a clear atomistic framework for magnesium–methane interaction; however, several limitations define the next phase of investigation. Most notably, explicit reaction pathway calculations have not yet been completed. While adsorption energies, hydrogen stabilization, and C–H bond

elongation strongly indicate surface-induced activation, a full nudged elastic band (NEB) analysis is required to quantify the methane dissociation barrier and determine the precise reduction in activation energy relative to the gas-phase pathway. Such calculations will convert the structural and thermodynamic evidence presented here into explicit kinetic parameters.

In addition, the current surface model represents an idealized Mg(0001) slab. Real combustion environments involve oxide layers, surface roughness, defects, and nanoparticle curvature. These features can modify adsorption strength, electronic redistribution, and dissociation energetics. Future work will therefore extend beyond flat slab geometries to include Mg nanoparticle models, stepped surfaces, and partially oxidized structures in order to capture realistic propulsion-relevant environments.

Building upon the atomistic results, microkinetic modeling will be performed to translate adsorption energetics and reaction barriers into reaction rate predictions and radical concentration evolution. Coupling these kinetics to computational fluid dynamics (CFD) simulations will allow evaluation of ignition delay, chamber pressure development, and thrust-related performance metrics in metalized methane combustion systems. This multiscale approach will directly connect atomic-scale activation mechanisms to propulsion-level performance.

Despite these limitations, the present results provide strong foundational insight. The Mg(0001) surface exhibits moderate methane adsorption (~−0.7 eV), largely orientation-independent behavior, and measurable elongation (4.78%) of the surface-facing C–H bond. In contrast, atomic hydrogen binds strongly (down to −2.64 eV), indicating thermodynamic stabilization of dissociation products. Electronic density redistribution further confirms that magnesium perturbs methane through surface-induced polarization rather than inert contact.

Together, these findings demonstrate that magnesium can electronically influence methane prior to combustion while simultaneously contributing energetic heat release through oxidation. The coexistence of bond weakening, hydrogen stabilization, and preserved metallic character establishes a coherent mechanistic basis for magnesium-assisted methane activation.

This work therefore provides an atomic-scale foundation for the metalized methane propulsion concept and defines a quantitative baseline for forthcoming reaction pathway calculations, kinetic modeling, and propulsion-scale performance evaluation.

VI. Acknowledgements

The author gratefully acknowledges Professor Michael Kinzel for his guidance, technical insight, and continued mentorship throughout the development of this research. The author also thanks the Computational Fluid and Aerodynamics Laboratory (CFAL), the College of Engineering, and the Department of Aerospace Engineering at Embry-Riddle Aeronautical University for their institutional and computational support.

This work was supported in part by the Embry-Riddle Office of Undergraduate Research through a Spark Travel Grant and an Undergraduate Research Scholarship, which are sincerely appreciated.

References

[1] Giannozzi, P., et al., "QUANTUM ESPRESSO: A Modular and Open-Source Software Project for Quantum Simulations of Materials," *Journal of Physics: Condensed Matter*, Vol. 21, No. 39, 2009, p. 395502. doi: 10.1088/0953-8984/21/39/395502

[2] Kohn, W., and Sham, L. J., "Self-Consistent Equations Including Exchange and Correlation Effects," *Physical Review*, Vol. 140, No. 4A, 1965, pp. A1133–A1138. doi: 10.1103/PhysRev.140.A1133

[3] Perdew, J. P., Burke, K., and Ernzerhof, M., "Generalized Gradient Approximation Made Simple," *Physical Review Letters*, Vol. 77, No. 18, 1996, pp. 3865–3868. doi: 10.1103/PhysRevLett.77.3865

[4] Monkhorst, H. J., and Pack, J. D., "Special Points for Brillouin-Zone Integrations," *Physical Review B*, Vol. 13, No. 12, 1976, pp. 5188–5192. doi: 10.1103/PhysRevB.13.5188

[5] Methfessel, M., and Paxton, A. T., "High-Precision Sampling for Brillouin-Zone Integration in Metals," *Physical Review B*, Vol. 40, No. 6, 1989, pp. 3616–3621. doi: 10.1103/PhysRevB.40.3616

[6] Villars, P., and Calvert, L. D., *Pearson's Handbook of Crystallographic Data for Intermetallic Phases*, ASM International, Materials Park, OH, 1991.

[7] Bengtsson, L., "Dipole Correction for Surface Supercell Calculations," *Physical Review B*, Vol. 59, No. 19, 1999, pp. 12301–12304. doi: 10.1103/PhysRevB.59.12301

[8] Payne, M. C., Teter, M. P., Allan, D. C., Arias, T. A., and Joannopoulos, J. D., "Iterative Minimization Techniques for ab initio Total-Energy Calculations," *Reviews of Modern Physics*, Vol. 64, No. 4, 1992, pp.

1045–1097.
doi: 10.1103/RevModPhys.64.1045
[9] Kresse, G., and Furthmüller, J., “Efficient Iterative Schemes for ab initio Total-Energy Calculations Using a Plane-Wave Basis Set,” *Physical Review B*, Vol. 54, No. 16, 1996, pp. 11169–11186.
doi: 10.1103/PhysRevB.54.11169
[10] Feibelman, P. J., “First-Principles Calculations of Surface Relaxation and Reconstruction,” *Progress in Surface Science*, Vol. 12, No. 4, 1982, pp. 287–407.
doi: 10.1016/0079-6816(82)90001-7
[11] Methfessel, M., Hennig, D., and Scheffler, M., “Trends of the Surface Relaxation, Surface Energy, and Work Function of the 4d Transition Metals,” *Physical Review B*, Vol. 46, No. 8, 1992, pp. 4816–4829.
doi: 10.1103/PhysRevB.46.4816
[12] Martin, R. M., *Electronic Structure: Basic Theory and Practical Methods*, Cambridge University Press, Cambridge, England, UK, 2004.
[13] Nørskov, J. K., Bligaard, T., Rossmeisl, J., and Christensen, C. H., “Towards the Computational Design of Solid Catalysts,” *Nature Chemistry*, Vol. 1, No. 1, 2009, pp. 37–46.
doi: 10.1038/nchem.121
[14] Hammer, B., and Nørskov, J. K., “Theoretical Surface Science and Catalysis—Calculations and Concepts,” *Advances in Catalysis*, Vol. 45, 2000, pp. 71–129.
doi: 10.1016/S0360-0564(02)45013-4
[15] Michaelides, A., Hu, P., and Alavi, A., “Alkane Activation and Dehydrogenation on Metal Surfaces,” *Journal of Chemical Physics*, Vol. 111, No. 3, 1999, pp. 1343–1352.
doi: 10.1063/1.479404
[16] Tait, S. L., Dohnálek, Z., Campbell, C. T., and Kay, B. D., “n-Alkanes on Metal Surfaces: Wetting, Interactions, and Desorption Kinetics,” *Journal of Chemical Physics*, Vol. 122, 2005, 164707.
doi: 10.1063/1.1884608
[17] Henkelman, G., Uberuaga, B. P., and Jónsson, H., “A Climbing Image Nudged Elastic Band Method for Finding Saddle Points and Minimum Energy Paths,” *Journal of Chemical Physics*, Vol. 113, No. 22, 2000, pp. 9901–9904.
doi: 10.1063/1.1329672
[18] Somorjai, G. A., and Li, Y., *Introduction to Surface Chemistry and Catalysis*, 2nd ed., Wiley, Hoboken, NJ, 2010.
[19] Kolasinski, K. W., *Surface Science: Foundations of Catalysis and Nanoscience*, 3rd ed., Wiley, Chichester, UK, 2012.
[20] Frenklach, M., and Wang, H., “Detailed Modeling of Soot Particle Nucleation and Growth,” *Symposium (International) on Combustion*, Vol. 23, 1991, pp. 1559–1566.
doi: 10.1016/S0082-0784(06)80426-8